Nanoscale

A Versatile Strategy for Controlled Assembly of Plasmonic Metal/Semiconductor Hemispherical Nano-heterostructure Arrays

Journal:	*Nanoscale*
Manuscript ID	NR-ART-05-2020-003551.R2
Article Type:	Paper
Date Submitted by the Author:	05-Aug-2020
Complete List of Authors:	Jia, Meng; University of Delaware College of Arts and Sciences, Chemistry and Biochemistry Zhang, Yuying; University of Delaware, Materials Science and Engineering Li, Zhengxin; University of Delaware, Chemistry and Biochemistry Crouch, Emma; University of Delaware, Department of Chemistry and Biochemistry Doble, Samantha; University of Delaware, Department of Chemistry and Biochemistry Avenoso, Joseph; University of Delaware, Department of Physics and Astronomy Yan, Han; University of Delaware, Department of Chemistry and Biochemistry Ni, Chaoying; University of Delaware, Materials Science and Engineering Gundlach, Lars; University of Delaware, Department of Chemistry and Biochemistry; University of Delaware, Department of Physics and Astronomy

Journal Name

ARTICLE TYPE

Cite this: DOI: 00.0000/xxxxxxxxxx

A Versatile Strategy for Controlled Assembly of Plasmonic Metal/Semiconductor Hemispherical Nano-heterostructure Arrays†

Meng Jia,[a] Yuying Zhang,[b] Zhengxin Li,[a] Emma Crouch,[a] Samantha Doble,[a] Joseph Avenoso,[c] Han Yan,[a] Chaoying Ni,[b] and Lars Gundlach *[ac]

Received Date
Accepted Date

DOI: 00.0000/xxxxxxxxxx

Recent advances in manipulating plasmonic properties of metal/semiconductor heterostructures have opened up new avenues for basic research and applications. Herein, we present a versatile strategy for the assembly of arrays of plasmonic metal/semiconductor hemispherical nano-heterostructures (MSHNs) with control over spacing and size of the metal/semiconductor heterostructure array, which can facilitate a wide range of scientific studies and applications. The strategy combines nanosphere lithography for generating the metal core array with solution-based chemical methods for the semiconductor shell that are widely available and kinetically controllable. Periodic arrays of Au/Cu_2O and Ag/Cu_2O heterostructures are synthesized to demonstrate the approach and highlight the versatility and importance of the tunability of plasmonic properties. The morphology, structure, optical properties, and elemental compositions of the heterostructures were analyzed. This strategy can be important for understanding and manipulating fundamental nanoscale solid-state physical and chemical properties, as well as assembling heterostructures with desirable structure and functionality for applications.

Introduction

Noble metal nanoparticles, in particular gold and silver nanoparticles, are the most commonly investigated plasmonic structures because their localized surface plasmon resonance (LSPR) lies in the visible-to-near-infrared regions and is easily accessible. The resonance frequency can be varied over a wide range by changing particle size, shape, composition, and arrangement.[1–3] LSPRs are collective excitations that can significantly alter light-matter interaction in materials. LSPRs are very short lived, on the order of tens of femtoseconds, and a significant amount of work has been done to couple LSPRs to other forms of excitations, e.g. excitons or hot electrons, in semiconductors that are long lived and can potentially be utilized for a wide range of applications such as solar energy conversion, photocatalysis, photovoltaics, electronics, and biotherapy.[4–13] Accordingly, numerous scientific studies have been devoted to the exploration of metal/semiconductor heterostructures, like Au/TiO_2, Ag/TiO_2, Au/ZnO, Au/Cu_2O, Au/CdS, Au/CdSe and Au/Fe_2O_3.[14–21]

Typically, wet chemistry for synthesizing the semiconductor shell of the heterostructures is performed in suspensions of metal nanoparticles. The presence of stabilizing capping agents (e.g. organic surfactants, PEG or biomolecular ligands) results in additional complexity of the system and can diminish the plasmonic effect by reducing the metal/semiconductor coupling.[22–24] Moreover, diffusion of larger nanoparticles in suspensions can lead to a spatial variation in concentration which renders the precise characterization difficult.[25,26] For several experimental methods it can be necessary to immobilize the nano-heterostructures on a solid substrate, e.g. electron spectroscopy and microscopy, as well as for some applications. In a number of reports, wet chemically synthesized nanostructures were deposited on solid substrates through self-assembly procedures such as drop-casting and floating-transfer, where the precise control of the interparticle spacing is challenging, if not impossible.[27–30] Single particle measurements or precise control of particle/particle interactions can hardly be achieved from particle suspensions. Precisely controllable arrays where coupling between individual particle can be adjusted are also important for several applications

[a] Department of Chemistry and Biochemistry, University of Delaware, Newark, Delaware, USA. E-mail: larsg@udel.edu
[b] Department of Material Science, University of Delaware, Newark, Delaware, USA.
[c] Department of Physics and Astronomy, University of Delaware, Newark, Delaware, USA.

† Electronic Supplementary Information (ESI) available: [Experimental details and characterization; size distribution calculations and supporting figures.]. See DOI: 00.0000/00000000.

that rely on the collective response of many core-shell nanoparticles like plasmonic nanoantennas, surface-enhanced Raman spectroscopy, and biochemical sensors.[31–34] Accordingly, for fundamental research in solid-state physics and chemistry and for a diverse set of potential and already realized applications, it is very important to develop a strategy for precisely arranging individual nano-heterostructures into well defined patterned arrays with high degree of regularity and uniformity.[35–37] Moreover, an array of metal nanoparticles on a substrate allows to apply electrochemical deposition for the growth of the semiconductor shell that can be controlled with much higher precision than regular wet chemistry, especially, in terms of the semi-shell thickness. Up-to-date lithography is the major tool for fabricating such periodic arrays and allows precise control of the size and shape of the nanostructures.[38,39] However, the costly and time-consuming preparation and requirement for major instrumentation have posed significant limitations for using conventional lithographic techniques like electron beam lithography (EBL) and focused ion beam (FIB) lithography. Consequently, only few examples of highly ordered metal/semiconductor nanoheterostructure arrays have been published.[40–42] Nanosphere lithography (NSL), which employs masks from self-assembled monolayers of close-packed colloidal spheres, has been proven to be a versatile technique for producing large well-ordered arrays of metal particles on the μm-up to mm-scale on different substrates[43–45]. Most of the recent studies of NSL were focused on either fabricating nanostructures with different morphologies or metal alloys.[46–50]

In this work, we demonstrate a flexible strategy to fabricate two-dimensional (2D) plasmonic metal/semiconductor hemispherical nano-heterostructures (MSHNs) by combining NSL and kinetically controllable and widely available solution-based chemical methods. Through this strategy, well-ordered Au/Cu_2O and Ag/Cu_2O heterostructure arrays were successfully fabricated on glass and fused silica substrates. The morphology, structural and optical properties, and elemental compositions of these heterostructures were experimentally analyzed. The proposed flexible approach enables the fabrication of plasmonic MSHNs with independent control of the metal nanohemispheres and semiconductor semi-shell components, which can facilitate scientific studies and help identify novel applications for plasmonic MSHNs.

Result and Discussion

Experimental Design

A schematic representation of our strategy for fabricating plasmonic MSHNs is illustrated in **Figure 1**. Arrays of plasmonic metal nanoparticles were fabricated using the NSL technique. Several approaches have been developed for the formation of self-assembled close-packed colloidal sphere monolayer masks including evaporation, controlled drop-casting, Langmuir-Blodgett techniques, floating-transfer techniques, and dip-coating.[51–54]

Here we use spin-coating that has proven to be a well controllable tool for preparing high-quality colloidal masks up to wafer-scale (**Figure 1a**).[55–57] Spin coating allows manipulation of several parameters like rotation speed, duration, and ramping stages to assemble homogeneous close-packed colloidal sphere monolayers. The substrates with the colloidal mask is subsequently coated in an electron-beam physical vapor deposition (PVD) system with a thin film of metal. Afterwards, sonication in toluene lifts off the colloidal mask from the substrate and a patterned array of metal nanoparticles in the form of triangular nanoprisms arranged in a hexagonal pattern is left on the substrate (**Figure 1b**). By annealing the substrates in ambient conditions, the remaining nanoprisms aggregated into nanohemispheres, as shown in **Figure 1c**. Our strategy utilizes the bare metal nanohemispheres on the substrate as a seeding template for successive semiconductor semi-shell growth. The experimental challenge of precise control of the semi-shell thickness requires slow growth of the semiconductor component. This requirement can be met by solution-based chemical methods, including chemical bath deposition and, especially, electrochemical deposition (**Figure 1d**). Chemical bath deposition is inarguable the simplest method for growth of the semiconductor semi-shell. Generally, the control of the shell growth rate can be achieved by manipulating various reaction parameters, such as the choice of chemical precursor, temperature, pH, and reaction time.[58] Electrochemical deposition represents a flexible and scalable method extensively used for growing nanomaterials with well defined morphology and chemical composition on a variety of substrates.[59] A slow growth rate can be achieved by controlling the current flow and the precursors' concentration. Both methods, yielded similar hemispherical nano-heterostructures. It is well known that the properties of the LSPR of the metal nanoparticles are strongly dependent on the size, shape, interpacticle spacing, and dielectric properties of the nanoparticles and the embedding media.[60] The NSL technique allows considerable freedom for controlling the size, shape, and interparticle spacing of the manufactured nanostructures by manipulating the size of the colloidal spheres, the metal film

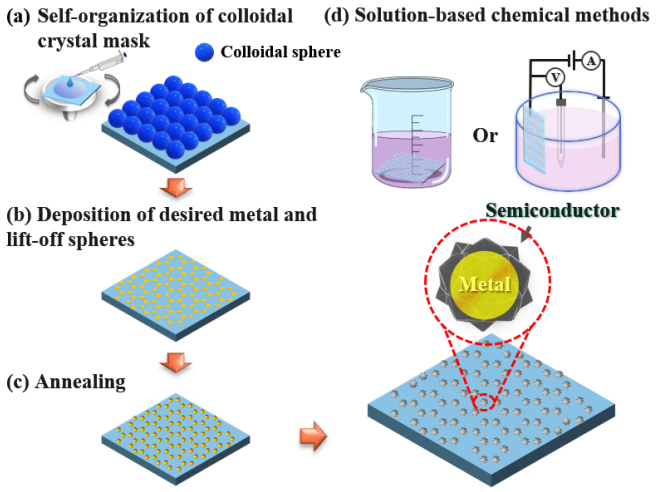

Fig. 1 Schematics of fabrication procedures for creating plasmonic MSHNs: (a) hexagonal close-packed PS monolayer mask was formed on the substrate through spin-coating, (b) metal nanoprisms formed after PVD and PS nanospheres lift-off, (c) metal nanoparticles presented after annealing, and (d) plasmonic metal/semiconductor MSHNs formed after the growth of semiconductor shell through solution-based chemical methods.

thickness, the incident angle of the metal deposition, and post-treatment methods like etching and heating.[44,45,61–65] Thus, the resonance frequency of the LSPR of the metal nanoparticle fabricated by NSL can be systematically tuned, for example throughout the visible, near-infrared, and mid-infrared regions for Ag nanoparticles.[43] The nano-heterostructures discussed here, lack the spherical symmetry of regular core/shell structures. However, immobilizing nanoparticles on a substrate also breaks the inversion symmetry for spherical particles. This can only be circumvented by immobilization in a surrounding matrix which is often problematic for spectroscopic and microscopic investigations. In addition, the hemispherical metal nanoparticles may offer distinct advantages in plasmonic properties compared to spherical metal nanoparticles. Theoretical studies suggest that hemispherical nanoparticles exhibit larger sensitivity to the incidence angle and polarization of radiation because of the broken symmetry compared to spherical nanoparticles, which provides additional parameters that can be exploited for fundamental studies and applications alike.[66–68] Quasistatic approximations have been used to study the distribution of the electric field of a single hemispherical metal core/semiconductor semi-shell nanoparticle on a substrate.[69,70] It has been shown that the plasmonic properties of the metal nanohemisphere depend on the dielectric permittivity of the substrate and the semi-shell, as well as the thickness of the semi-shell. The localization effect of the shell on the plasmon generally results in a red-shift that depends on, and can be systematically tuned by, the semi-shell thickness.[71] Therefore, the ability to precisely control the semi-shell thickness and the large range of available semiconductor materials through solution-based chemical methods is a significant advantage of the method presented here. Among all of the MSHNs that have been reported so far, Au/Cu_2O represents one of the most extensively studied combinations since Cu_2O, as a p-type semiconductor, has a very strong effect on the plasmonic response of the embedded Au nanoparticle.[72–74] Thus, we exemplify our new fabrication strategy by preparing and characterizing periodic arrays of Au/Cu_2O MSHNs first. We then show the versatility of this strategy by modifying the size of the Au nanoparticles and the thickness of the Cu_2O semi-shell, followed by the preparation and characterization of Ag/Cu_2O MSHNs.

Preparation and Morphology of the Au/Cu_2O array

Figure 2(a - d) show representative scanning electron microscopy (SEM) images of the well-ordered 2D Au/Cu_2O MSHN array that follows the sequence of the fabrication approach in the schematics in (**Figure 1**). As shown in **Figure 2a**, a monolayer of hexagonal closed-packed polystyrene (PS) spheres with a diameter of 500 nm is assembled on the glass substrate via spin-coating. In the spin-coating process, we start depositing the colloidal suspension of PS spheres on the center of a glass substrate at a slow rotational speed of 100 rpm (phase I). The suspension droplet spreads out to form a circle on the substrate. Then, the rotation speed of the substrate was gradually increased to 400 rpm and the suspension further spread out and covered a large circular area (phase II). The suspension film thickness is given by the equilibrium between centrifugal force and viscous shear force. The film thickness is further reduced by evaporation until it is equal to the diameter of the PS spheres, at which point capillary forces have a significant impact on particle aggregation (phase III). An image of the spherical PS monolayer mask formed on the glass substrate is shown in **Figure S1**. The sub-wavelength thickness of the monolayer leads to a distinct diffraction pattern where large regions of uniform diffraction indicate large well-ordered PS monolayers.

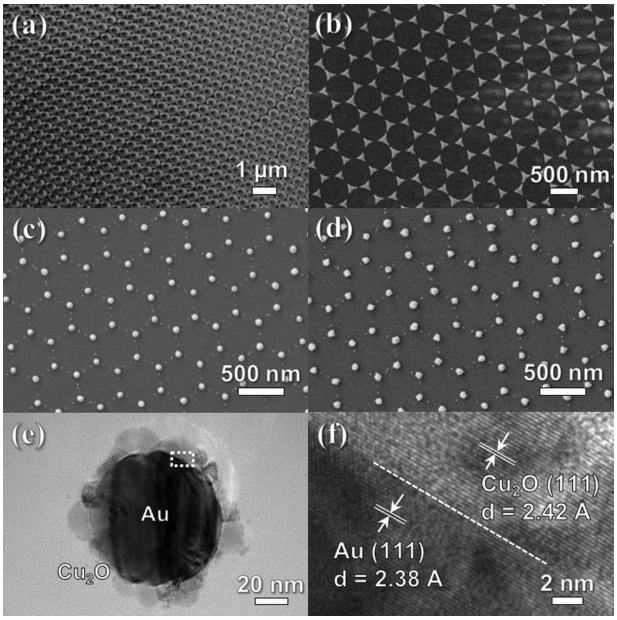

Fig. 2 SEM images of (a) 2D 500 nm PS nanosphere mask, (b) as deposited Au nanoprisms, (c) annealed Au nanoparticles and (d) Au/Cu_2O heterostructure arrays; TEM image of (e) a single Au/Cu_2O heterostructure and (f) HR-TEM image of the interface between Au and Cu_2O.

Spin coating of the PS mask was followed by deposition of a 20 nm-thick Au film through PVD at a rate of 1 Å/s and subsequent removal of the PS sphere mask via sonication in toluene. **Figure 2b** shows the remaining Au nanoprism arrays on the substrate. Annealing of the substrate at 550°C in ambient atmosphere for 30 min converted the gold nanoprisms into spherical nanoparticles shown in **Figure 2c**. While the annealing temperature was lower than the melting point of bulk Au, it was still sufficiently high to cause surface melting and the formation of spherical nanoparticles due to surface tension.[63]

The Cu_2O nanocrystalline shell was synthesized by room-temperature hydrolysis (**Figure 2d**). This synthetic method was based on a redox reaction in copper(II) sulfate solution, that was modified from the approach developed by Kuo and coworkers,[75] in which Cu_2O synthesis was performed on stabilized Au nanoparticles from suspension. $Cu(OH)_4^{2-}$ was formed after the addition of excess NaOH. The reducing agent then reduced it to Cu_2O nanocrystals. Due to the small lattice mismatch (*vide infra*) and the chemical stability, Au nanocrystals served as an effective seeding template for the growth of Cu_2O poly-crystalline nanocrystals. By controlling the precursor concentration and reaction temperature, a crystalline Cu_2O shell was gradually formed at a slow rate. The size distribution of fabricated nanoparticle arrays was

extracted from the SEM images using the ImageJ software. Histograms of the size distributions of several samples created by the NSL technique with the corresponding Gaussian fits are shown in **Figure 3**. The Au nanoparticle in the arrays had an in-plane diameter of 72 ± 4 nm. Compared with the calculated in-plane diameter of 80 ± 6 nm of the Au/Cu_2O heterostructures, the Cu_2O shell thickness is estimated to be ∼ 10 nm. Detailed calculation of the nanoparticle in-plane diameter can be found in the SI. The morphology of the samples was further characterized by transmission electron microscopy (TEM). **Figure 2e** confirms a diameter of 73 nm for the Au core and a thickness of ∼ 10 nm for the Cu_2O semi-shell. The hemispherical shape of the Au/Cu_2O heterostructures can be observed in a TEM image of a side view of a scratched-off particle, as shown in (**Figure S3**). A thickness of below 20 nm for the Cu_2O semi-shell could easily be achieved with this procedure, which normally is challenging and requires synthesis at ice/water temperatures with a chemical bath deposition method.[76] It should be noted that the interface between Au and Cu_2O is very homogeneous. The lattice fringes in the Au/Cu_2O nanocrystal are clearly visible in the high-resolution TEM (HR-TEM) images and the observed interplanar spacing of 2.38 Å and 2.42 Å corresponds to the (111) plane of Au and Cu_2O, respectively (**Figure 2f**). The crystalline Cu_2O grown on the Au nanocrystal shows a high degree of structural homogeneity at the interface due to the same face cubic crystal structure and the small (111) plane lattice mismatch of ∼ 4.7 % (Cu_2O (a= 4.269 Å) and Au (a= 4.065 Å)).

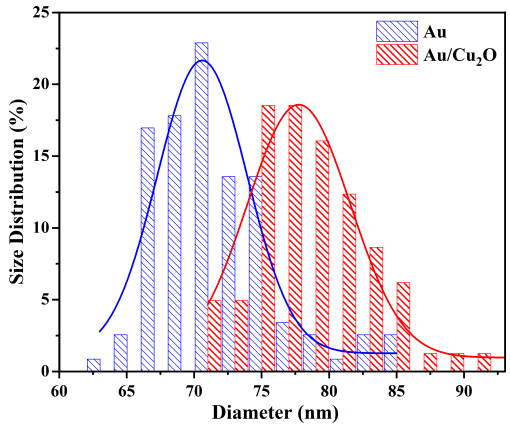

Fig. 3 Histograms of size distribution of Au nanoparticles (blue) and Au/Cu_2O heterostructures (red) with the corresponding Gaussian fits.

Crystal Structural and Spectroscopic Characterization

To study the interaction between Au and Cu_2O domains, we compared the optical properties of isolated Cu_2O nanocrystals, Au nanoparticles, and the Au/Cu_2O heterostructures (**Figure 4a**). The isolated Cu_2O nanocrystals were prepared by a electrochemical deposition method (see details in the Supporting Information). The absorption spectrum of Cu_2O nanocrystal showed a sharp adsorption edge at ∼ 510 nm. This energy matches the bandgap of p-type Cu_2O. The spectrum of the Au nanoparticle array is dominated by the plasmon resonance. The change of the in-plane shape from triangular to circular via annealing during the preparation procedure results in a blue-shift of the LSPR absorption to ∼ 535 nm accompanied by a narrowing of the peak (**Figure S2**).[77] The spectrum of the heterostructures shows a combination of the Cu_2O band transition and the plasmon resonance. However, compared with isolated Au nanoparticles, the plasmon resonance is broadened and red-shifted to 574 nm, indicating strong electronic interaction between the Au and Cu_2O domains. The observation is consistent with the general trend of a red-shift of the plasmon peak due to the confinement by the shell.[28,76,78] A similar broadening of the LSPR peak has been observed in Au/Cu_2O nanoparticles previously.[76]

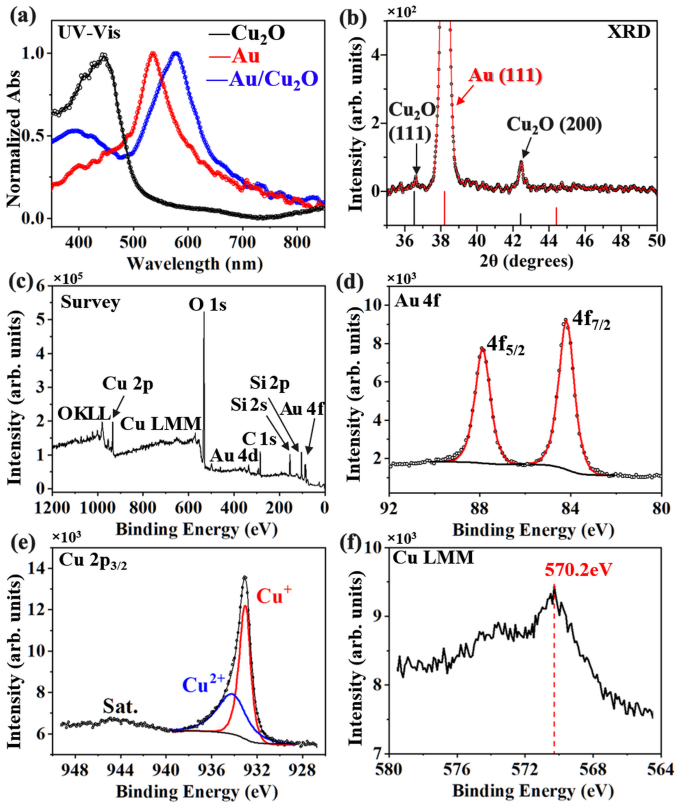

Fig. 4 (a) UV-Vis of Au nanoparticles arrays (red) and Au/Cu_2O heterostructures (blue); (b) Expended XRD pattern of the Au/Cu_2O heterostructures with the standard positions of Au (JCPDS 04-0784, red) and Cu_2O (JCPDS 05-0667, black); XPS (c) survey, (d) Au 4f, (e) Cu 2p(3/2) and (f) Cu LMM spectra of Au/Cu_2O heterostructures at a base pressure of 3 × 10^{-8} Torr.

Further structural characterization of the Au/Cu_2O heterostructures was performed by X-ray diffraction (XRD) (**Figure 4b**). The prominent peak at 38.22° correspond to the (111) plane of face-centered cubic Au (JCPDS card no. 04-0784), and the weaker features at 36.58 and 42.43° can be assigned to the (111) and (200) of face-centered cubic Cu_2O (JCPDS card no. 05-0667). Au nanoparticles showed a preferred orientation along the Au (111) plane that can be related to the annealing step during fabrication. The diffraction intensity from the Au phase is found to be higher than that from the Cu_2O phase, indicating a higher quantity of Au in the individual heterostructures due to the thin Cu_2O semi-shell. The XRD result agrees well with the

lattice spacing observed in the HR-TEM results. The elemental composition of the MSHNs arrays was characterized by X-ray photoelectron spectroscopy (XPS) at a base pressure of 3×10^{-8} Torr. The survey spectrum clearly shows Cu 2p and Au 4f peaks from the Au/Cu_2O heterostructures and additional features from the glass substrate (**Figure 4c**). High-resolution XPS analysis of core-level spectra (Au 4f, Cu $2p_{3/2}$) and of the Auger spectrum (Cu LMM) is required to characterize the oxidation states of the domains (Au and Cu_2O) in the heterostructure. As shown in **Figure 4d**, the Au 4f spectrum is composed of a well-resolved metallic (Au^0) doublet with 7/2 and 5/2 spins separated by 3.67 eV (**Figure 4d**).[79] The Cu $2p_{3/2}$ spectrum shows a main broad peak and a very weak satellite feature (**Figure 4e**). The main broad peak presents two components: the main component at 933.0 eV assigned to Cu^+ ions characteristic of the Cu_2O phase, and the lower intensity component at higher binding energy (934.3 eV) corresponding to Cu^{2+} ions. Though the XRD pattern does not show any evidence for the CuO phase, the presence of a Cu^{2+} state in the XPS spectra indicates that oxidation is present at the surface of the Cu_2O semi-shell and it likely forms a thin amorphous outer shell. As demonstrated in previous XPS studies, the binding energy of the Auger peak is a good fingerprint for the copper oxidation state. The binding energy of the main Auger peak measured at 570.2 eV presents further confirmation that Cu_2O is the main component.[80] As the Cu^{2+} is the more energetically favorable state compared to the Cu^+ state, the surface of the Cu_2O nanocrystals can easily be oxidized to form a sub-nanometer thin CuO layer.[81,82] This oxide layer protects the Cu_2O nanocrystals from further degradation under ambient conditions.[83]

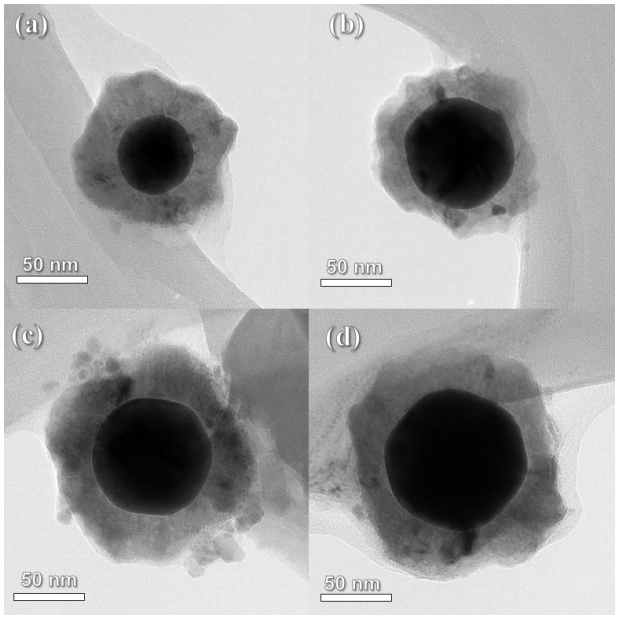

Fig. 5 TEM images of Au/Cu_2O heterostructures with tunable Au nanoparticle diameter from ~58 nm to ~100 nm which correspond to different deposited Au film thicknesses of (a) 15, (b) 20, (c) 60, and (d) 100 nm using the same size of diameter nanosphere mask. The magnification is kept same in for the convenience of direct comparison. The thickness of Cu_2O shell is ~25 nm for all the heterostructures.

Size and Shell-Thickness Control of Au/Cu_2O Heterostructure

To demonstrate the level of control that this strategy provides, we study the plasmonic properties in dependence of core size and shell thickness. As discussed in the previous section, the size of

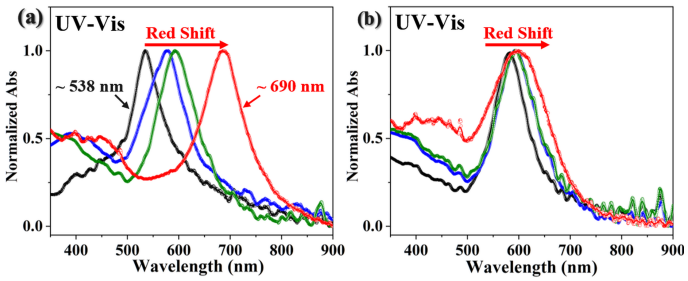

Fig. 6 Tunable plasmonic properties of Au/Cu_2O heterostructures with independent metal core and semiconductor shell control. (a) UV-Vis spectra of Au/Cu_2O heterostructures with same Au nanoparticle size (71 nm, black) and different thickness of Cu_2O shell of ~10 (blue), ~25 (green), and ~60 nm (red). (b) UV-Vis spectra of Au/Cu_2O heterostructures with similar Cu_2O thickness (~25 nm) and different Au nanoparticle diameter of 58 (black), 71 (blue), 83 (green) and 100 nm (red).

the metal nanoparticles fabricated by NSL can be controlled by changing the diameter of the nanospheres that form the mask and by the thickness of the deposited metal. Here we varied the thickness of the Au film from 15 nm to 100 nm while keeping the diameter of the nanospheres constant. **Figure 5** exemplifies the control over the metal core size enabled by this strategy. A series of TEM images of Au/Cu_2O MSHNs with similar thickness for the Cu_2O semi-shell (~25 nm) and Au nanoparticle diameter ranging from ~58 nm to ~100 nm. Similarly, by varying the precursor concentration and growth time the semi-shell thickness can be tuned. TEM images of Au/Cu_2O MSHNs with different shell thicknesses are shown in **Figure S8**. These structures have the same Au core diameter but Cu_2O shell thickness ranging from ~10 nm to ~60 nm. The core size and shell thickness can be independently controlled over a wide range and can enable a high degree of tunability of the electronic and optical properties. **Figure 6a** shows spectra of Au/Cu_2O heterostructures with the same size Au core of 70 nm and increasing Cu_2O thickness and **Figure 6b** shows the UV-Vis absorption of Au/Cu_2O nanoparticles with increasing core diameter and constant shell thickness of 25 nm. The LSPR absorption of the Au/Cu_2O heterostructures undergoes a red-shift of 574 nm, 605 nm and 690 nm as the thickness of the Cu_2O shell increases respectively from 10 nm to 25 nm and 60 nm as shown in (**Figure 6a**). If the core diameter is changed successively and the shell thickness is kept constant, a similar red-shift is observed. However, the LSPR absorption is more sensitive to the shell thickness than to the core diameter, cf. **Figure 6a and S9**. Thus small variations in the shell thickness have a large effect and the successive red-shift is less obvious because of unintended small variations in shell thickness. The steady red-shift of the LSPR absorption of pure Au nanoparticles from 529 nm to 561 nm upon increasing the Au nanoparticle diameter from 58 nm to 100 nm is shown in **Figure S9**. It is obvious that the plasmonic properties of heterostructures fabricated through this strategy can be tailored to a wide range of wavelength window

in a very accurate manner which could facilitate versatile applications.

Preparation and Characterization of Ag/Cu_2O Heterostructure

In addition to Au/Cu_2O heterostructures, we demonstrate our approach for an Ag/Cu_2O MSHN array in **Figure 7**. **Figure 7(a, b)** show SEM images of well-ordered 2D Ag nanoparticles and Ag/Cu_2O heterostructures. Histograms of the size distributions of the Ag nanoparticles and Ag/Cu_2O heterostructures with the corresponding Gaussian fits are shown in **Figure S4**. The dimensions of the Ag/Cu_2O heterostructures are similar to the Au/Cu_2O heterostructures presented earlier. Since Ag nanoparticles are less

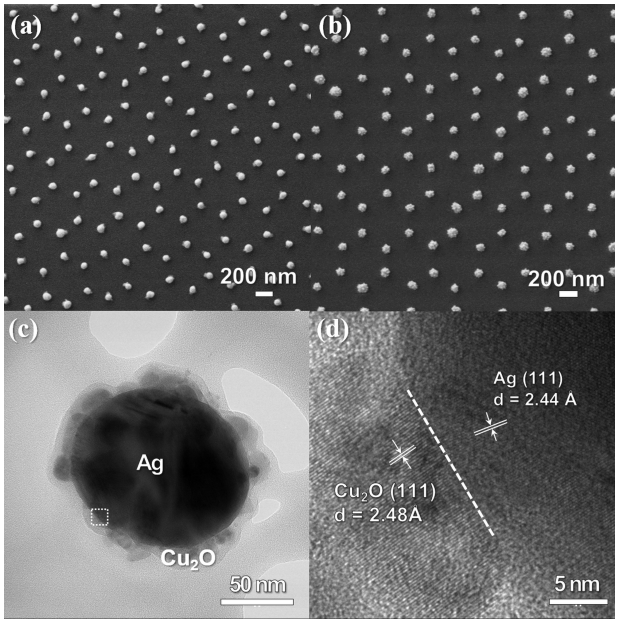

Fig. 7 SEM images of (a) annealed Ag nanoparticles and (b) Ag/Cu_2O heterostructure arrays; TEM image of (c) a single Ag/Cu_2O heterostructure and (d) HR-TEM image of the cross-section of Ag/Cu_2O showing the core-shell interface.

stable compared to Au nanoparticles annealing of Ag nanoparticles was achieved already at 300 °C which was significantly lower than for Au nanoparticles. **Figure 7(c, d)** shows TEM and HR-TEM images of the Ag/Cu_2O heterostructure interface that are of comparable quality as shown above for Ag/Cu_2O. UV-vis spectra of Ag nanoparticles and Ag/Cu_2O heterostructures are shown in **Figure S5** revealing again the expected red-shift for the core-shell structure. To confirm the elemental identification, we carry out energy dispersive X-ray spectroscopy (EDS) measurements on a single heterostructure (**Figure S6**). Additional examples, including samples prepared on fused silica substrate, are provided in the Supporting Information (**Figure S7**) to show the flexibility of our strategy.

Conclusions

Our fabrication strategy presents a new approach to prepare periodic arrays of plasmonic metal/semiconductor hemispherical nano-heterostructures that is very flexible in terms of substrate, metal and semiconductor domains. It provides independent control of metal core diameter, semiconductor semi-shell thickness, and interparticle spacing that enables a high degree of tunability of heterostructures to tailor materials properties and functionality in a very accurate manner. The importance of such precise dimensional control has been highlighted by showing plasmonic property dependence of semiconductor semi-shell on the as-prepared Au/Cu_2O heterostructures, which can be critical for the fundamental understanding in solid-state physics and chemistry alike, as well as for the optimization for their application in devices. Since semiconductor shells can be converted to related chemical and biochemical compounds, it is also noteworthy that this approach can offer a general method to create a wide range of heterostructure arrays with the desired functionality and thus provide versatile nanoscale building blocks by a bottom-up approach.

Conflicts of interest

There are no conflicts to declare.

Acknowledgments

This material is partly based upon work supported by the U.S. Department of Energy, Office of Science, Office of Basic Energy Sciences, Office of Energy Research, under Awards Number DE-SC0016288 (L.G.). The authors gratefully acknowledge the funding of NSF 1428149 for Thermo Scientific K-Alpha instruments. We thank Dr. Yong Zhao, Dr. Jennifer Sloppy, and Thomas Barkley in the University of Delaware's W. M. Keck Center for Advanced Microscopy and Microanalysis for the electron microscopy measurements and Gerald Poirier and Dr. Jing Qu in the University of Delaware's Advanced Materials Characterization Lab for the XRD characterization.

Notes and references

1 J. A. Schuller, E. S. Barnard, W. Cai, Y. C. Jun, J. S. White and M. L. Brongersma, *Nat. Mater.*, 2010, **9**, 193–204.
2 S. V. Boriskina, H. Ghasemi and G. Chen, *Mater. Today*, 2013, **16**, 375–386.
3 S. Linic, P. Christopher and D. B. Ingram, *Nat. Mater.*, 2011, **10**, 911–921.
4 M. L. Brongersma, N. J. Halas and P. Nordlander, *Nat. Nanotechnol.*, 2015, **10**, 25–34.
5 M. Moskovits, *Nat. Nanotechnol.*, 2015, **10**, 6–8.
6 B. Y. Zheng, H. Zhao, A. Manjavacas, M. McClain, P. Nordlander and N. J. Halas, *Nature communications*, 2015, **6**, 1–7.
7 K. Wu and T. Lian, *Chem. Soc. Rev.*, 2016, **45**, 3781–3810.
8 J. Wang, W. Lin, X. Xu, F. Ma and M. Sun, *Chem. Rec.*, 2018, **18**, 481–490.
9 H. A. Atwater and A. Polman, in *Materials For Sustainable Energy: A Collection of Peer-Reviewed Research and Review Articles from Nature Publishing Group*, World Scientific, 2011, pp. 1–11.
10 R. Jiang, B. Li, C. Fang and J. Wang, *Adv. Mater.*, 2014, **26**, 5274–5309.
11 M. Wang, M. Ye, J. Iocozzia, C. Lin and Z. Lin, *Adv. Sci.*, 2016, **3**, 1600024.

12 T.-H. Tran and T.-D. Nguyen, *Pract. Appl. Biomed. Eng.*, 2013, 311.

13 N. Wu, *Nanoscale*, 2018, **10**, 2679–2696.

14 X.-F. Wu, H.-Y. Song, J.-M. Yoon, Y.-T. Yu and Y.-F. Chen, *Langmuir*, 2009, **25**, 6438–6447.

15 T. Hirakawa and P. V. Kamat, *J. Am. Chem. Soc.*, 2005, **127**, 3928–3934.

16 K. K. Haldar, T. Sen and A. Patra, *J. Phys. Chem. C*, 2008, **112**, 11650–11656.

17 L. Zhang, D. A. Blom and H. Wang, *Chem. Mater.*, 2011, **23**, 4587–4598.

18 S. Lambright, E. Butaeva, N. Razgoniaeva, T. Hopkins, B. Smith, D. Perera, J. Corbin, E. Khon, R. Thomas, P. Moroz, A. Mereshchenko, A. Tarnovsky and M. Zamkov, *ACS Nano*, 2013, **8**, 352–361.

19 M. Lukosi, H. Zhu and S. Dai, *Front. Chem. Sci. Eng.*, 2016, **10**, 39–56.

20 K. M. AbouZeid, M. B. Mohamed and M. S. El-Shall, *Small*, 2011, **7**, 3299–3307.

21 W.-T. Chen, T.-T. Yang and Y.-J. Hsu, *Chem. Mater.*, 2008, **20**, 7204–7206.

22 H. Kang, J. T. Buchman, R. S. Rodriguez, H. L. Ring, J. He, K. C. Bantz and C. L. Haynes, *Chem. Rev.*, 2018, **119**, 664–699.

23 D. R. Baer, J. E. Amonette, M. H. Engelhard, D. J. Gaspar, A. S. Karakoti, S. Kuchibhatla, P. Nachimuthu, J. Nurmi, Y. Qiang, V. Sarathy *et al.*, *Surf. Interface Anal.*, 2008, **40**, 529–537.

24 S. Mourdikoudis, R. M. Pallares and N. T. Thanh, *Nanoscale*, 2018, **10**, 12871–12934.

25 J. Guan, B. Wang and S. Granick, *ACS Nano*, 2014, **8**, 3331–3336.

26 R. Metzler, J.-H. Jeon, A. G. Cherstvy and E. Barkai, *Phys. Chem. Chem. Phys.*, 2014, **16**, 24128–24164.

27 M. Brust and C. J. Kiely, *Colloids Surf., A*, 2002, **202**, 175–186.

28 H. Li, W. Ali, Z. Wang, M. F. Mideksa, F. Wang, X. Wang, L. Wang and Z. Tang, *Nano Energy*, 2019, **63**, 103873.

29 C. Li, S. Wang, H. Li, M. Saqib, C. Xu and Y. Jin, *Iscience*, 2019, **17**, 267–276.

30 C. Li, C. Xu, D. Cahen and Y. Jin, *Sci. Rep.*, 2019, **9**, 1–9.

31 R. Adato, A. A. Yanik, J. J. Amsden, D. L. Kaplan, F. G. Omenetto, M. K. Hong, S. Erramilli and H. Altug, *Proc. Natl. Acad. Sci. U.S.A.*, 2009, **106**, 19227–19232.

32 S. Dodson, M. Haggui, R. Bachelot, J. Plain, S. Li and Q. Xiong, *J. Phys. Chem. Lett.*, 2013, **4**, 496–501.

33 K.-H. Su, Q.-H. Wei, X. Zhang, J. Mock, D. R. Smith and S. Schultz, *Nano letters*, 2003, **3**, 1087–1090.

34 R. Elghanian, J. J. Storhoff, R. C. Mucic, R. L. Letsinger and C. A. Mirkin, *Science*, 1997, **277**, 1078–1081.

35 A. P. Alivisatos, *Science*, 1996, **271**, 933–937.

36 C. Collier, T. Vossmeyer and a. J. Heath, *Annu. Rev. Phys. Chem.*, 1998, **49**, 371–404.

37 Y. Xia, B. Gates, Y. Yin and Y. Lu, *Adv. Mater.*, 2000, **12**, 693–713.

38 N. C. Lindquist, P. Nagpal, K. M. McPeak, D. J. Norris and S.-H. Oh, *Rep. Prog. Phys.*, 2012, **75**, 036501.

39 M. Scuderi, M. Esposito, F. Todisco, D. Simeone, I. Tarantini, L. De Marco, M. De Giorgi, G. Nicotra, L. Carbone, D. Sanvitto *et al.*, *J. Phys. Chem. C*, 2016, **120**, 24314–24323.

40 P. Viste, J. Plain, R. Jaffiol, A. Vial, P. M. Adam and P. Royer, *ACS nano*, 2010, **4**, 759–764.

41 P. Thiyagarajan, H.-J. Ahn, J.-S. Lee, J.-C. Yoon and J.-H. Jang, *Small*, 2013, **9**, 2341–2347.

42 L. Mehrvar, M. Sadeghipari, S. Tavassoli, S. Mohajerzadeh and M. Fathipour, *Sci. Rep.*, 2017, **7**, 1–13.

43 T. R. Jensen, M. D. Malinsky, C. L. Haynes and R. P. V. Duyne, *J. Phys. Chem. B*, 2000, **104**, 10549–10556.

44 C. L. Haynes and R. P. V. Duyne, *J. Phys. Chem. B*, 2001, **105**, 5599–5611.

45 P. Colson, C. Henrist and R. Cloots, *J. Nanomater.*, 2013, **2013**, 1–19.

46 G. Zhang, D. Wang and H. Möhwald, *Nano Lett.*, 2007, **7**, 127–132.

47 W. Ingram, S. Larson, D. Carlson and Y. Zhao, *Nanotechnology*, 2016, **28**, 015301.

48 W. Wang, Y. Ma and L. Qi, *Adv. Funct. Mater.*, 2017, **27**, 1603653.

49 B. Ai and Y. Zhao, *Nanophotonics*, 2018, **8**, 1–26.

50 X. Liang, R. Dong and J. C. Ho, *Advanced Materials Technologies*, 2019, **4**, 1800541.

51 K. Chen, C. Durak, J. R. Heflin and H. D. Robinson, *Nano Lett.*, 2007, **7**, 254–258.

52 N. Marquestaut, A. Martin, D. Talaga, L. Servant, S. Ravaine, S. Reculusa, D. M. Bassani, E. Gillies and F. Lagugné-Labarthet, *Langmuir*, 2008, **24**, 11313–11321.

53 C. Li, G. Hong and L. Qi, *Chem. Mater.*, 2010, **22**, 476–481.

54 A. S. Dimitrov and K. Nagayama, *Langmuir*, 1996, **12**, 1303–1311.

55 P. Jiang and M. J. McFarland, *J. Am. Chem. Soc.*, 2004, **126**, 13778–13786.

56 P. Jiang, T. Prasad, M. J. McFarland and V. L. Colvin, *Appl. Phys. Lett.*, 2006, **89**, 011908.

57 P. Colson, R. Cloots and C. Henrist, *Langmuir*, 2011, **27**, 12800–12806.

58 G. Hodes, *Chemical Solution Deposition of Semiconductor Films*, CRC press, 2002.

59 M. Aliofkhazraei and A. S. H. Makhlouf, *Handbook of Nanoelectrochemistry: Electrochemical Synthesis Methods, Properties, and Characterization Techniques*, Springer, 2016.

60 U. Kreibig and M. Vollmer, *Optical Properties of Metal Clusters*, Springer Science & Business Media, 2013, vol. 25.

61 J. C. Hulteen, D. A. Treichel, M. T. Smith, M. L. Duval, T. R. Jensen and R. P. Van Duyne, *J. Phys. Chem. B*, 1999, **103**, 3854–3863.

62 C. L. Haynes, A. D. McFarland, M. T. Smith, J. C. Hulteen and R. P. Van Duyne, *J. Phys. Chem. B*, 2002, **106**, 1898–1902.

63 B. Tan, C. Sow, T. Koh, K. Chin, A. Wee and C. Ong, *J. Phys. Chem. B*, 2005, **109**, 11100–11109.

64 L. S. Live and J.-F. Masson, Photonics North 2009, 2009, p. 73861M.
65 Q. Zhang, S. Ghosh, S. Samitsu, X. Peng and I. Ichinose, *J. Mater. Chem.*, 2011, **21**, 1684–1688.
66 P. Albella, B. Garcia-Cueto, F. González, F. Moreno, P. C. Wu, T.-H. Kim, A. Brown, Y. Yang, H. O. Everitt and G. Videen, *Nano Lett.*, 2011, **11**, 3531–3537.
67 J. Sanz, D. Ortiz, R. Alcaraz De La Osa, J. Saiz, F. González, A. Brown, M. Losurdo, H. Everitt and F. Moreno, *J. Phys. Chem. C*, 2013, **117**, 19606–19615.
68 T. Attanayake, M. Premaratne and G. P. Agrawal, *Plasmonics*, 2015, **10**, 1453–1466.
69 S. Scherbak, O. Shustova, V. Zhurikhina and A. Lipovskii, *Plasmonics*, 2015, **10**, 519–527.
70 S. Scherbak and A. Lipovskii, *J. Appl. Phys.*, 2016, **119**, 163106.
71 S. Scherbak, N. Kapralov, I. Reduto, S. Chervinskii, O. Svirko and A. Lipovskii, *Plasmonics*, 2017, **12**, 1903–1910.
72 B. Rai, *Solar Cells*, 1988, **25**, 265–272.
73 B. D. Yuhas and P. Yang, *J. Am. Chem. Soc.*, 2009, **131**, 3756–3761.
74 Z. Li, M. Jia, S. Doble, E. Hockey, H. Yan, J. P. Avenoso, D. Bodine, Y. Zhang, C. Ni, J. T. Newberg and L. Gundlach, *ACS Appl. Mater. Interfaces*, 2019, **11**, 40490–40502.
75 C.-H. Kuo, T.-E. Hua and M. H. Huang, *J. Am. Chem. Soc.*, 2009, **131**, 17871–17878.
76 D.-Y. Liu, S.-Y. Ding, H.-X. Lin, B.-J. Liu, Z.-Z. Ye, F.-R. Fan, B. Ren and Z.-Q. Tian, *J. Phys. Chem. C*, 2012, **116**, 4477–4483.
77 A. Colombelli, D. Lospinoso, A. Taurino and M. G. Manera, *Journal of Materials Chemistry C*, 2019, **7**, 13818–13828.
78 B. Lu, A. Liu, H. Wu, Q. Shen, T. Zhao and J. Wang, *Langmuir*, 2016, **32**, 3085–3094.
79 J. F. Moulder, *Physical Electronics*, 1995, 230–232.
80 L. Martin, H. Martinez, D. Poinot, B. Pecquenard and F. Le Cras, *J. Phys. Chem. C*, 2013, **117**, 4421–4430.
81 M. Yin, C.-K. Wu, Y. Lou, C. Burda, J. T. Koberstein, Y. Zhu and S. O'Brien, *J. Am. Chem. Soc.*, 2005, **127**, 9506–9511.
82 C.-K. Wu, M. Yin, S. O'Brien and J. T. Koberstein, *Chem. Mater.*, 2006, **18**, 6054–6058.
83 B. Balamurugan, B. Mehta and S. Shivaprasad, *Appl. Phys. Lett.*, 2001, **79**, 3176–3178.